APL Photonics

High performance thin-film lithium niobate modulator on a silicon substrate using periodic capacitively loaded traveling-wave electrode

Cite as: APL Photonics **7**, 026103 (2022); https://doi.org/10.1063/5.0077232
Submitted: 31 October 2021 • Accepted: 16 January 2022 • Published Online: 02 February 2022

Gengxin Chen, Kaixuan Chen, Ranfeng Gan, et al.

High performance thin-film lithium niobate modulator on a silicon substrate using periodic capacitively loaded traveling-wave electrode

Cite as: APL Photon. 7, 026103 (2022); doi: 10.1063/5.0077232
Submitted: 31 October 2021 • Accepted: 16 January 2022 •
Published Online: 2 February 2022

Gengxin Chen,[1] Kaixuan Chen,[2,3] Ranfeng Gan,[2] Ziliang Ruan,[1] Zong Wang,[2] Pucheng Huang,[2] Chao Lu,[4] Alan Pak Tao Lau,[5] Daoxin Dai,[1] Changjian Guo,[2,3,4,a)] and Liu Liu[1,a)]

AFFILIATIONS

[1] State Key Laboratory for Modern Optical Instrumentation, Centre for Optical and Electromagnetic Research, International Research Center for Advanced Photonics, East Building No. 5, Zijingang Campus, Zhejiang University, Hangzhou 310058, China

[2] Guangdong Provincial Key Laboratory of Optical Information Materials and Technology, South China Academy of Advanced Optoelectronics, Sci. Bldg. No. 5, South China Normal University, Higher-Education Mega-Center, Guangzhou 510006, China

[3] National Center for International Research on Green Optoelectronics, South China Normal University, Guangzhou 510006, China

[4] Photonics Research Center, Department of Electronic and Information Engineering, The Hong Kong Polytechnic University, Hong Kong, China

[5] Photonics Research Center, Department of Electrical Engineering, The Hong Kong Polytechnic University, Hong Kong, China

[a)] **Authors to whom correspondence should be addressed:** changjian.guo@coer-scnu.org and liuliuopt@zju.edu.cn

ABSTRACT

Thin-film lithium niobate (TFLN) based traveling-wave modulators maintain simultaneously excellent performances, including large modulation bandwidth, high extinction ratio, low optical loss, and high modulation efficiency. Nevertheless, there still exists a balance between the driving voltage and modulation bandwidth. Here, we demonstrate an ultra-large bandwidth electro-optic modulator without compromising the driving voltage based on the TFLN platform on a silicon substrate, using a periodic capacitively loaded traveling-wave electrode. In order to compensate the slow-wave effect, an undercut etching technique for the silicon substrate is introduced to decrease the microwave refractive index. Our demonstrated devices represent both low optical and low microwave losses, which leads to a negligible optical insertion loss of 0.2 dB and a large electro-optic bandwidth with a roll-off of 1.4 dB at 67 GHz for a 10 mm-long device. A low half-wave voltage of 2.2 V is also achieved. Data rates up to 112 Gb s^{-1} with PAM-4 modulation are demonstrated. The compatibility of the proposed modulator to silicon photonics facilitates its integration with matured silicon photonic components using, e.g., hybrid integration technologies.

I. INTRODUCTION

Optical communication systems are now widely used all around the world to cope with the ever-increasing need for data transmission. The transmission rate of the data signal highly relies upon the electrical-to-optical data conversion. Optical modulators, when integrated with laser sources, can translate signals from the electrical domain to the optical domain at a high speed, which become essential components in long-haul telecommunication networks,[1] optical quantum memories,[2] radio-frequency (RF) photonics,[3] and data-center communications.[4] One of the most simple and cost-effective approaches is to internally modulate the driving current of a semiconductor laser.[5] However, this sort of direct modulation is intrinsically limited in both modulation bandwidth and extinction ratio and also suffers from modulation chirp. On the other hand, external electro-optic (EO) modulators can

present better modulation performances and have been developed in various material platforms. Pure silicon-based modulators,[6] due to the absence of the Pockels effect, rely on the carrier injection or depletion in p–n junctions that are integrated into the optical waveguide. This leads to an inherent trade-off between the modulation efficiency and optical loss. The integration of silicon or plasmonic material with organic EO polymers, called silicon–organic hybrid[7,8] or plasmonic–organic hybrid modulators,[9,10] can benefit from ultra-high EO coefficients of some engineered polymers, but their stability still needs improvement. They often suffer from high losses as well. Indium phosphate (InP) based modulators can achieve high digital data rates,[11] but their intrinsic modulation nonlinearity, as well as high cost, limits their applications to a wide range.

Lithium niobate (LN) EO modulators, due to their outstanding material properties, including good temperature stability, wide transparency window, and highly efficient linear Pockels effect, have been widely used in long-haul optical communications.[12] Traditional bulk LN EO modulators, by means of proton exchange or titanium diffusion,[13] are limited in performances due to the fact that the waveguide core is weakly guided with a low refractive index contrast (<0.2). Its optical mode is large, which limits the minimal spacing between the modulation electrodes and, hence, the minimal driving voltage.[14] Nevertheless, the invention of ultra-low loss thin-film lithium niobate (TFLN) waveguide platforms can overcome this fundamental limitation, which provides a high index contrast using low refractive index materials, e.g., air or silicon dioxide, as the cladding layer. EO modulators based on etched ridge waveguides on the TFLN platform exhibit excellent performances of small footprint, low half-wave voltage (V_π), and high bandwidth beyond 100 GHz, as compared to traditional bulk LN EO modulators.[15,16]

EO modulators simultaneously having a low V_π and a large EO bandwidth are important for applications spanning from RF analog links to digital optical communication networks. However, there is an intrinsic trade-off between V_π and the EO bandwidth. The greater the V_π is, the shorter the length of the modulation section L should be and hence the larger the EO bandwidth can be. The challenge to maintain a large EO bandwidth with a low driving voltage is how to simultaneously retain properties, including low optical losses, low RF losses, perfect impedance matching, and perfect velocity matching between the optical and RF waves. The key modulation efficiency metric, called the half-wave voltage length product ($V_\pi L$), is mainly limited by the electrode gap. The smaller the electrode gap is, the lower the $V_\pi L$ will be. On the other hand, a small electrode gap will introduce additional optical losses due to metal absorption and decreases EO bandwidths as well under perfect impedance and velocity matching due to the increased RF losses. In order to break this compromise, a periodic capacitively loaded traveling-wave (CLTW) electrode structure has been proposed on the TFLN platform.[17] The basic idea here is to use a very wide signal electrode to largely decrease the RF losses (which leads to a large bandwidth). In the meantime, T-shaped periodic structures are added in between the ground and signal electrodes to maintain a small electrode gap (and hence a low $V_\pi L$) without largely increasing the distributed capacitance (keeping the impedance matching). However, this structure would largely decrease the phase speed of the RF signal (i.e., the slow-wave effect).[17] In order to maintain the index matching, a low permittivity substrate, e.g., quartz, was employed.

In this paper, we demonstrate TFLN based EO modulators using a CLTW electrode on a silicon substrate. This device allows a small electrode gap to achieve a low $V_\pi L$ (~2.20 V cm) value without

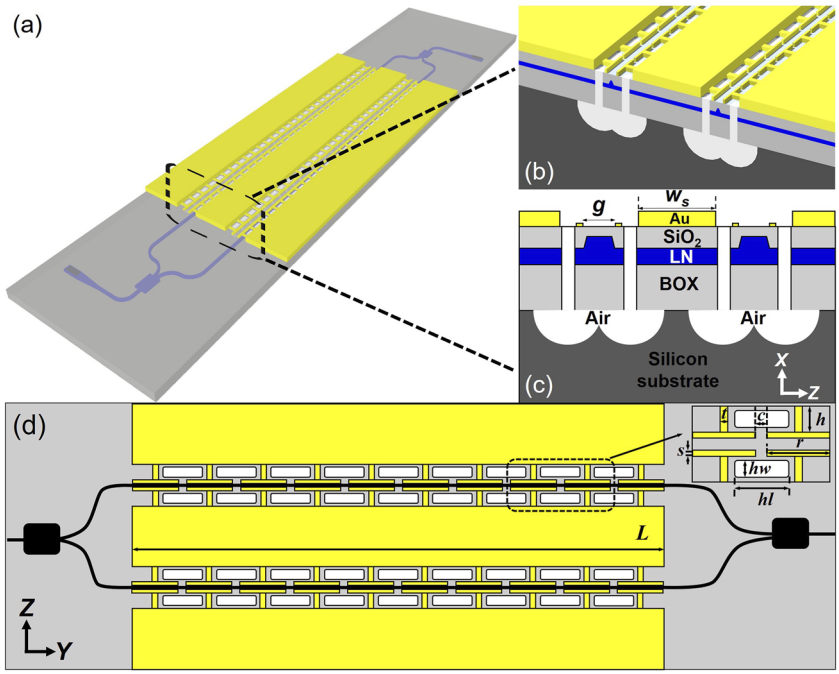

FIG. 1. Proposed EO modulator on a silicon substrate using the CLTW electrode. (a) 3D view of the whole structure. (b) 3D view and (c) 2D view of the cross-sectional structure of the modulation section. (d) Top view of the MZI structure.

additional optical absorption losses. Meanwhile, the silicon undercut etching technique is introduced to achieve velocity matching between the optical and RF waves, which also helps to reduce RF absorption losses from the semiconducting substrate.[17] Compared with EO modulators on the TFLN platform with regular traveling-wave electrodes on a silicon substrate,[15] the proposed EO modulator shows excellent high-frequency performance with only a 1.4 dB roll-off at 67 GHz. In addition, the proposed devices show an ultra-low optical insertion loss of 0.2 dB and a large static extinction ratio of >20 dB. On–off keying (OOK) modulation up to 100 Gbit s^{-1} and PAM-4 modulation up to 112 Gbit s^{-1} are successfully achieved with a dynamic extinction ratio of >9.7 dB.

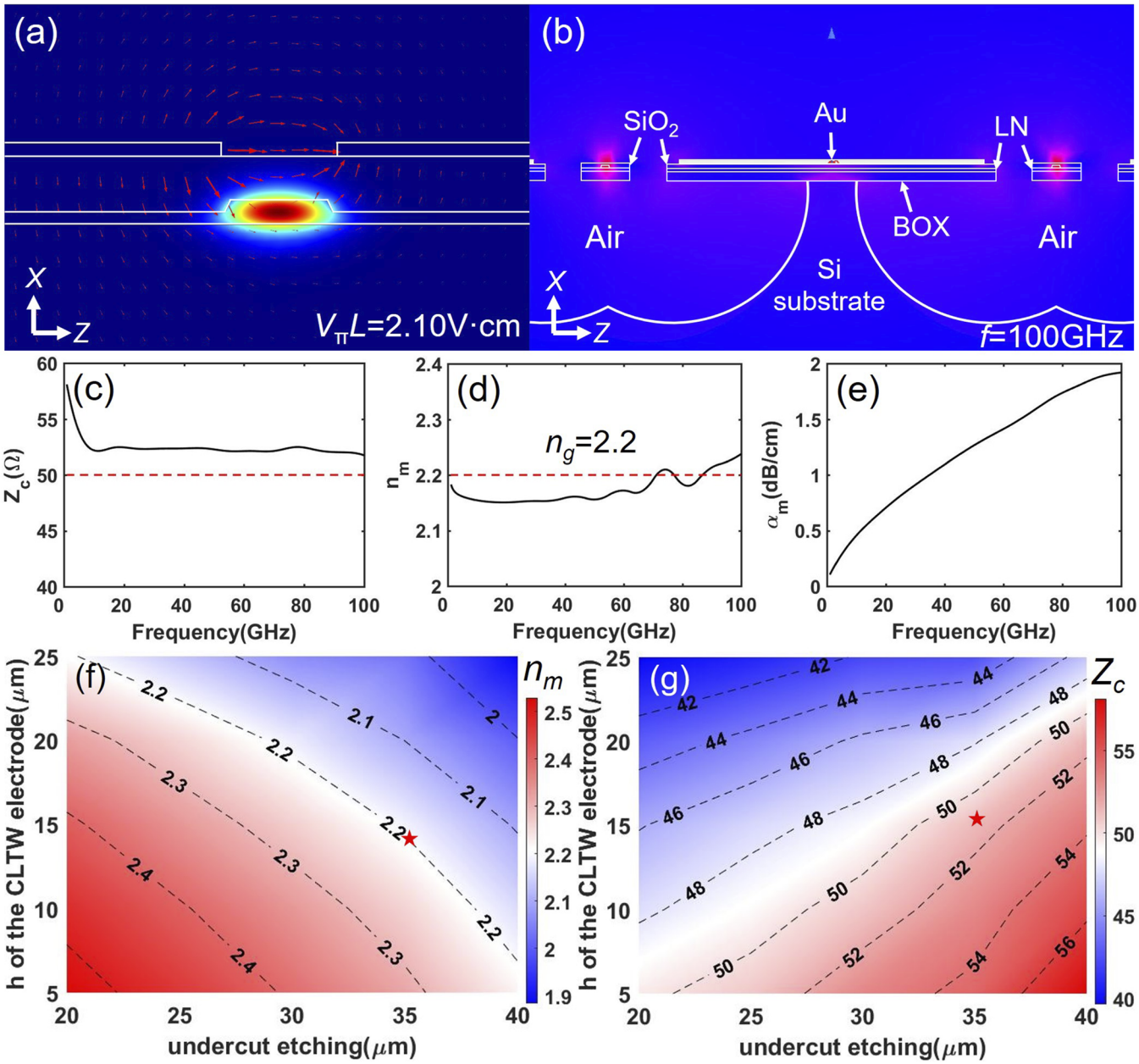

FIG. 2. (a) Simulated TE optical mode profile and static electrical field distribution. $V_\pi L$ = 2.10 V cm can be extracted here. (b) Simulated RF mode profile at a RF frequency of 100 GHz. Simulated frequency-dependent results of (c) characteristic impedance Z_c, (d) RF effective index n_m, and (e) RF loss α_m. The two red dashed lines in (c) and (d) correspond to the source/load impedance 50 Ω and the optical group index n_g, respectively. Effects of undercut etching and h on (f) n_m and (g) Z_c at 70 GHz. The optimal point is marked as a star.

II. DEVICE DESIGN AND FABRICATION

Figure 1(a) shows a three-dimensional (3D) view of the proposed TFLN based EO modulators using a CLTW electrode on an undercut etched silicon substrate. The device is fabricated on a commercial x-cut LN-on-insulator (LNOI) wafer with a 3 μm thick buried oxide (BOX) layer and a 400 nm thick TFLN layer. The waveguide at the modulation section has a ridge height of 200 nm, i.e., half of the TFLN total thickness, and a width of 1.5 μm. Grating couplers (GCs) are used as fiber-to-chip interfaces.[18] Multimode interferometers made also on TFLN are used as 3 dB couplers for the Mach–Zehnder interferometer (MZI) structure. The CLTW electrode based on a classic coplanar-line structure with some periodically loaded T-segment structures is adopted in the proposed device, in which optical and RF waves propagate collinearly. In the regular TW electrode design, the high characteristic RF loss α_0 of 0.75 dB cm^{-1} GHz$^{-1/2}$[17] is the dominant source of limiting the EO bandwidth performance. As mentioned in Sec. I, by properly designing the parameters of the CLTW electrode, this RF loss can be largely decreased. Figures 1(b) and 1(c) show cross-sectional views of the EO modulators. It should be noted that the gap g between CLTW electrodes has a major effect on the modulation efficiency $V_\pi L$. Thanks to the 900 nm thick silicon oxide (SiO_2) over-cladding layer on top of the TFLN waveguides, excessive optical absorption losses are avoided even if a small gap of g = 1.8 μm is adopted. The thickness of the T-segment electrodes is set to 200 nm to ensure an easy lift-off process for these high-resolution structures, and the thickness of the unloaded electrodes is 1.1 μm, which is at a good balance between the performance and cost.[19] The unloaded signal electrode has a width of w_s = 75 μm, which is designed large to reduce the conductor losses for the RF waves. In order to compensate the slow-wave effect introduced by the periodic T-segment structures, the silicon substrate is partially removed, leaving an air hole beneath the TFLN waveguides, as shown in Figs. 1(c) and 1(d). This effectively decreases the permittivity of the material seen by the RF wave. The parameters of the CLTW electrode are carefully designed to ensure the impedance and index matching, which gives (r, c, s, t, h, hw, hl) = (47, 3, 2, 5, 15, 9, 39) μm, and a 35 μm undercut etching of the silicon substrate is optimal.

A multi-physics field solver based on the finite element algorithm (COMSOL) was used to simulate the electrical and optical modes of the structure. $V_\pi L$ = 2.10 V cm can be derived with a low optical propagation loss of ~0.04 dB/cm for the fundamental transverse-electrical (TE) mode, as shown in Fig. 2(a). Figure 2(b) shows the RF field distributions. Unlike EO modulators using the regular TW electrode, the RF field here is localized around the gap of the loaded T-segments, instead of the wide unloaded signal electrode. This helps us increase the overlap of the electrical and optical fields and hence a low $V_\pi L$. The frequency-dependent characteristic impedance Z_c, the RF effective index n_m, and the RF loss α_m obtained from the simulations are shown in Figs. 2(c)–2(e), respectively. Figures 2(f) and 2(g) further show effects of different undercut etching and h of the CLTW electrode on the RF effective index n_m and characteristic impedance Z_c, respectively. Obviously, these two figures play an important role for achieving the index and impedance matching. Nearly perfect impedance and index matching can be achieved up to 100 GHz in this design. The RF loss can be expressed as $\alpha_m = \alpha_0(f)^{1/2}$, where f is the

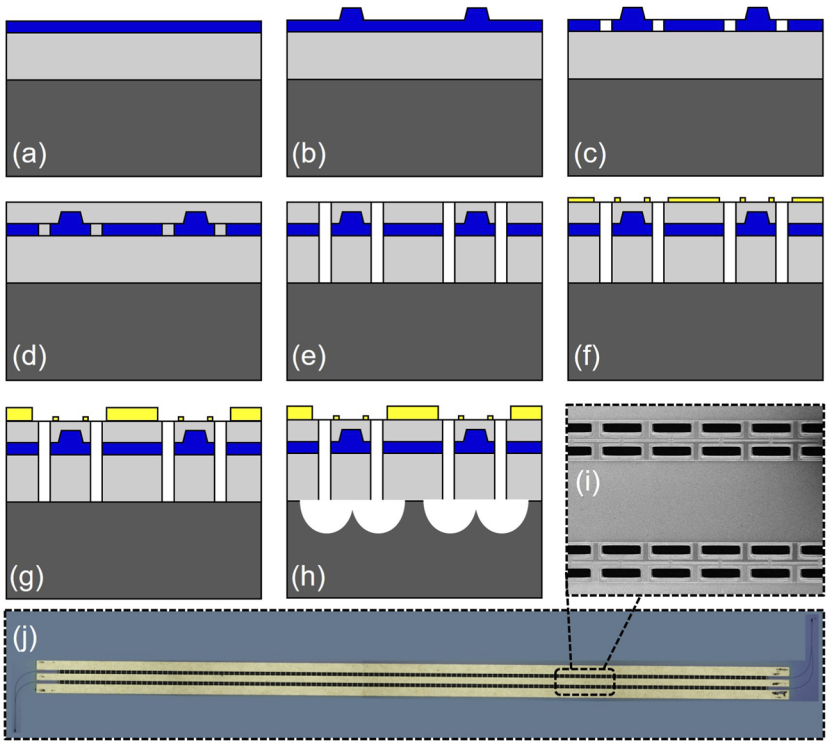

FIG. 3. Process flow of the proposed EO modulator: (a) initial LNOI wafer, (b) definition of passive components on LNOI, (c) LN hole etching, (d) SiO_2 over-cladding deposition, (e) SiO_2 hole etching to the silicon substrate, (f) first level metal patterning for the T-segments, (g) second level metal patterning for the unload TW electrodes, (h) isotropic silicon etch to partially remove the substrate, (i) scanning electron microscopy image of the CLTW electrode, and (j) optical image of the whole fabricated device.

RF frequency and α_0 is the frequency independent characteristic RF loss. Here, α_0 of 0.19 dB cm^{-1} GHz$^{-1/2}$ can be drawn from the data shown in Fig. 2(e), which is much lower than that of the regular TW electrode based modulators as mentioned above.

The proposed EO modulators using the designed CLTW electrode were fabricated using the process flow shown in Figs. 3(a)–3(h). First, an LNOI wafer consisting of 400 nm thick x-cut TFLN on a 725 μm thick silicon substrate with a 3 μm thermal oxide layer (i.e., the BOX layer) was patterned using an electron beam lithography system (Raith VOYAGER) on a 300 nm thick resist (ma-N 2403). Then, a 200 nm thick LN layer was removed using Ar plasma by means of inductively coupled plasma reactive ion etching (ICP-RIE) technology with an etching rate of ~80 nm/min. Holes between the T-segments and the unload TW electrodes were then patterned using ultra-violet contact lithography, and the residual 200 nm LN layer was etched. The device was then covered with a 900 nm thick SiO_2 layer deposited by plasma enhanced chemical vapor deposition. Subsequently, the holes were again patterned, and the over-cladding SiO_2 layer and the BOX layer were etched to expose the silicon substrate. Next, the metal structures made of gold were fabricated using two lift-off processes for the periodic T-segments and the unloaded TW electrodes, respectively. Finally, the holes were patterned for the third time, and isotropic silicon dry etching using ICP-RIE technology was performed to remove the silicon substrate beneath the modulation section. Figures 3(i) and 3(j) show some images of the CLTW electrode and the whole fabricated device, respectively.

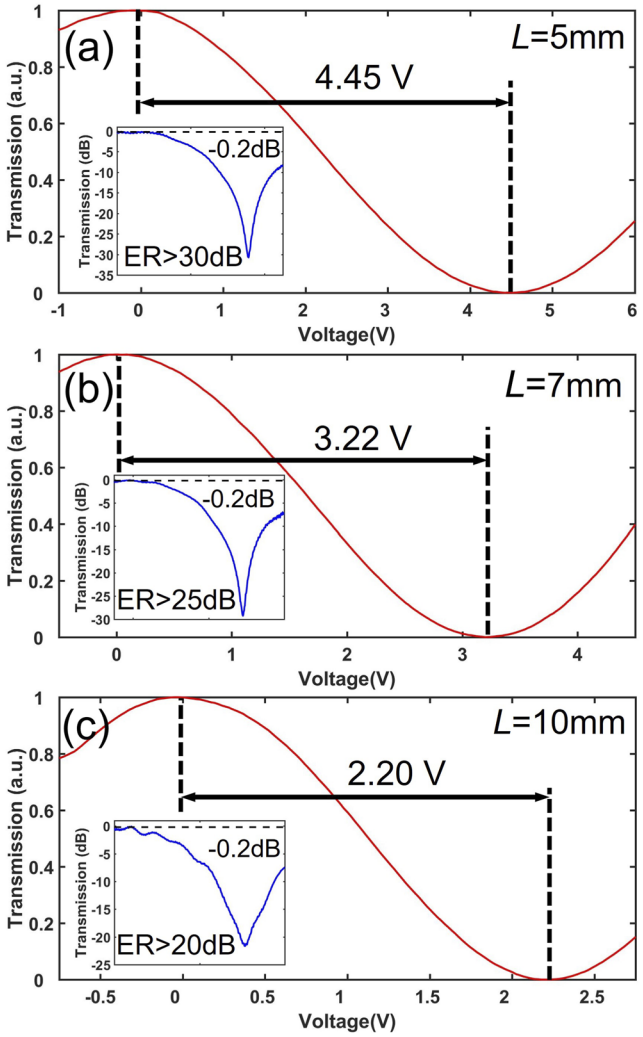

FIG. 4. Normalized optical transmissions of the fabricated modulators as a function of the applied voltage for (a) a 5 mm long device, (b) a 7 mm long device, and (c) a 10 mm long device. The V_π value for each device is also marked. The insets show the measured transmissions in a logarithmic scale showing the insertion losses and ERs of the corresponding devices.

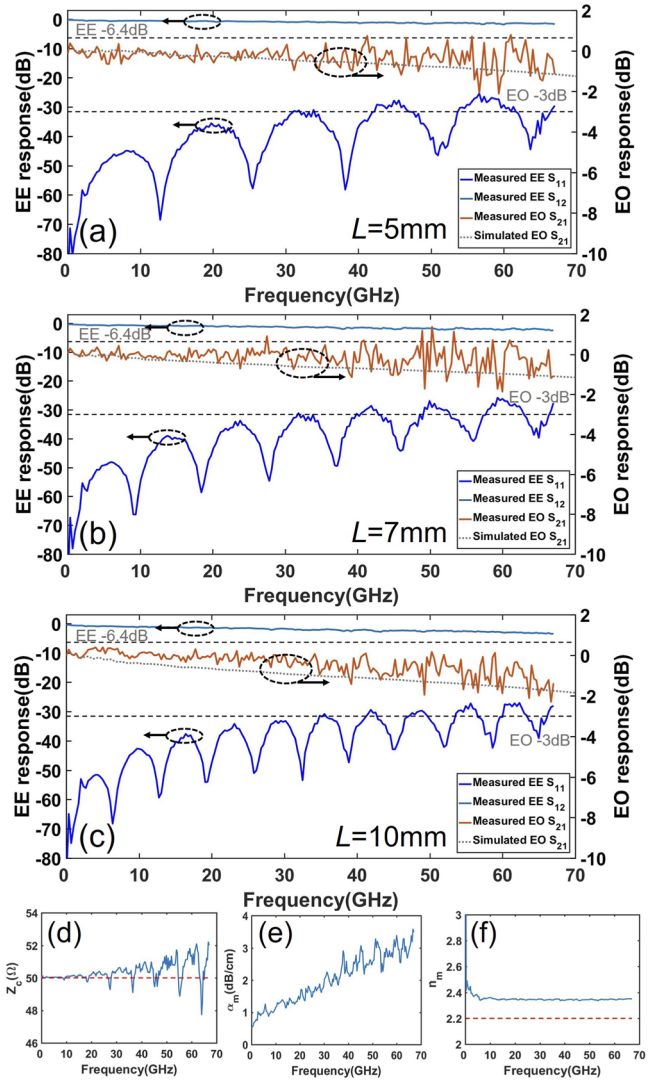

FIG. 5. Measured EE reflection S_{11}, EE transmission S_{12}, measured EO S_{21}, and calculated EO S_{21} for (a) 5 mm, (b) 7 mm, and (c) 10 mm long devices. Deduced (d) characteristic impedance Z_c, (e) RF loss α_m, and (f) RF effective index n_m.

III. MEASUREMENT AND ANALYSIS

The fabricated EO modulators with modulation section lengths of 5, 7, and 10 mm were characterized. The laser light was coupled in and out through a pair of GCs. The coupling loss of the GC was first measured using a reference structure consisting of two such GCs and a short straight waveguide. The total insertion loss including the device and the coupling GCs is 8.2 dB at the peak coupling wavelength, and the on-chip loss of ~0.2 dB for the longest device (10 mm) can be deduced. Thanks to the thick SiO_2 overcladding layer to block the metal absorptions, this loss nearly came alone from the propagation loss of the TFLN waveguide (about 0.15 dB/cm). Figure 4 shows the half-wave voltage V_π measurements for the three devices with a 100 kHz triangular voltage sweep. The V_π values for the 5, 7, and 10 mm long devices are 4.45, 3.22, and 2.20 V, respectively, corresponding to a $V_\pi L$ of 2.22, 2.25, and 2.20 V cm, respectively, which are consistent with the simulation results in Fig. 2. The insets in Figs. 4(a)–4(c) show transmissions of the devices with a static voltage sweep, demonstrating measured extinction ratios (ERs) of >30, >25, and >20 dB, respectively. It is believed that the improvement of ERs can be achieved by optimizing fabrication imperfections, such as a better write-field stitching and metal electrode alignment.

Next, the EO and electrical–electrical (EE) responses of the fabricated devices were characterized. As shown in Figs. 5(a)–5(c), the measured EE transmissions S_{12} show an ultra-low roll-off of less than 1.7, 2.4, and 3.5 dB at 67 GHz for the 5, 7, and 10 mm long devices, respectively. Moreover, the EE reflection S_{11} is below −25 dB over the entire measured frequency range for all the devices. The smooth and flat transmission S_{12}, as well as the low reflection S_{11}, indicates that the conditions for a good impedance matching and ultra-low RF losses have been achieved, which can also be seen from the deduced characteristic impedances Z_c and RF losses, as plotted in Figs. 5(d) and 5(e), respectively. The characteristic RF loss $\alpha_0 = 0.36$ dB cm^{-1} GHz$^{-1/2}$ for the measured device can also be fitted from Fig. 5(e). This value is about twice the simulation results mentioned above. The additional RF loss probably comes from either the residual silicon substrate or the quality of the deposited gold film. Figure 5(f) shows the deduced RF index n_m, where one can find that there still exists a slight index mismatching of ~0.15 between the optical and RF waves. Longer isotropic undercut etching for the silicon substrate should be done to further reduce the RF index. The small signal EO responses S_{21} were further measured using a 70-GHz photodetector (Finisar XPDV3120). One RF probe was used to deliver the modulation signal, and the other was used to provide a 50 Ω termination. The 3 dB EO modulation bandwidths of the 5, 7, and 10 mm long devices are all greater than 67 GHz beyond the measurement limits of our network analyzer. The measured EO S_{21} curves are also well matched to our calculated curves, using the fitted data in Figs. 5(d)–5(f). Despite the slight index mismatch, the longest fabricated device (10 mm) still shows smooth EO modulation responses with a roll-off of only 1.4 dB at 67 GHz.

We, then, characterized the performance of the 10 mm long device for high-speed data transmissions. Figures 6(a) and 6(b) show the optical eye diagrams for the OOK modulation at 80 and 100 Gb s^{-1}, respectively. We also tested the PAM-4 modulation

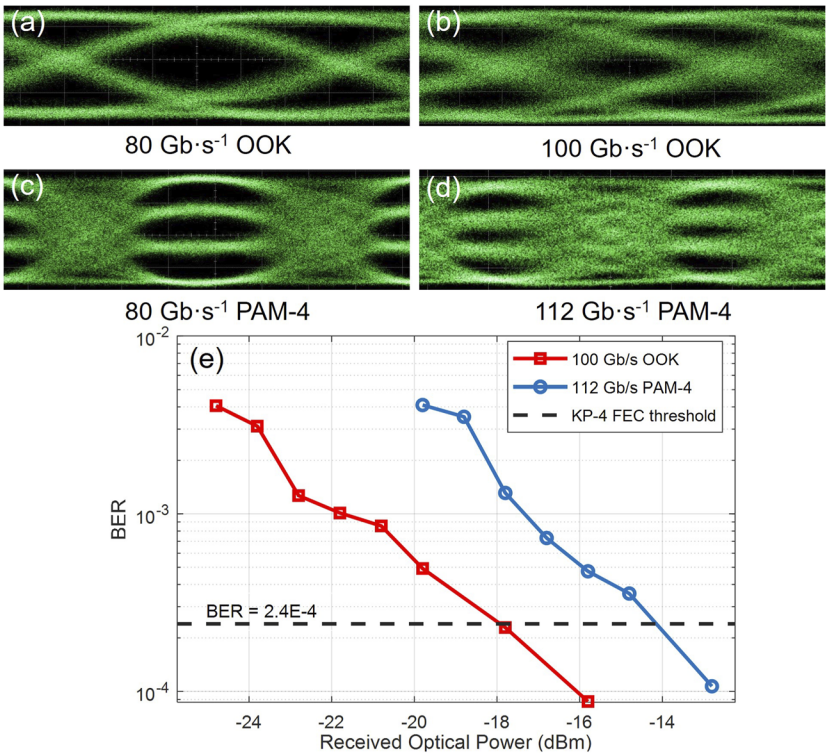

FIG. 6. High-speed data transmission experiments on the fabricated EO modulator of 10 mm length. Measured optical eye diagrams for the OOK format at data rates of (a) 80 Gb s^{-1} and (b) 100 Gb s^{-1}. Measured optical eye diagrams for the PAM-4 format at data rates of (c) 40 Gbaud (80 Gb s^{-1}) and (d) 56 Gbaud (112 Gb s^{-1}). (e) Measured B2B BERs at different received optical power values for 56 Gbaud PAM-4 and 100 Gb s^{-1} OOK.

TABLE I. Comparison of several performance metrics for EO modulators on the TFLN platform.

Devices	Insert. loss (dB)	V_π (V)	Len. of mod. sec. (mm)	EO S_{21} roll-off
SOI-TFLN[17]	2.5	5.10	5	−3 dB (at 67 GHz)
SOI-TFLN[22]	7.6	13.4	5	−1.5 dB (at 106 GHz)
SiN-TFLN[23]	NM[a]	3.87	8	−3 dB (at 40 GHz)
TFLN[15]	0.2	2.3	10	−2.1 dB (at 67 GHz)
	0.5	1.4	20	−3 dB (at 45 GHz)
TFLN[18] (Q)[b]	1.5	2.3	10	−0.8 dB (at 50 GHz)
	1.5	1.3	20	−1.8 dB (at 50 GHz)
TFLN[21] (Q)[b]	6[c]	3.4	5	−1.3 dB (at 67 GHz)
This work	0.2	2.2	10	−0.76 dB (at 50 GHz) −1.4 dB (at 67 GHz)

[a]NM, not mentioned.
[b]Q, Quartz substrate.
[c]The value is calculated from the total on-chip loss of 17 dB and the coupling loss of 11 dB.

format at 40 Gbaud (80 Gb s^{-1}) and 56 Gbaud (112 Gb s^{-1}), as shown in Figs. 6(c) and 6(d), respectively. During the measurement, the data were generated using an arbitrary wave generator (AWG) with an analog bandwidth of ~35 GHz (Micram DAC10004). The eye diagrams were recorded using a sampling oscilloscope with a bandwidth of 65 GHz (Agilent 81600D). The dynamic ERs are all better than 9.7 dB in all the above-mentioned eye diagrams. The back-to-back (B2B) bit-error rates (BERs) of 100 Gb/s OOK and 56 Gbaud PAM-4 signals were further measured using a pre-amplified receiver that consisted of a variable optical attenuator, an Erbium doped fiber amplifier with a noise figure of about 4.3 dB, an optical band pass filter with a 3-nm bandwidth, a 70-GHz photodetector, and a real-time oscilloscope with a 59-GHz analog bandwidth (Lecroy Labmaster 10Zi). The BERs were calculated offline using digital signal processing algorithms including down-sampling, timing phase synchronization, and a 11-tap least-mean-square equalizer. One can find that for all cases, the BER can drop below the KP-4 forward error correction (FEC) threshold, as shown in Fig. 6(e). No error floor is observed in the measured power range. It is worthwhile to note that the data transmission performance shown here is still limited by bandwidths of the equipment, as mentioned above. Table I summarizes key performances of some demonstrated EO modulators based on the TFLN platform. One can find that the proposed device here shows better EO responses (a lower roll-off) with a similar modulation efficiency and insertion loss, as compared to the state-of-the-art TFLN modulator using the conventional TW electrode on a silicon substrate.[15] It also shows a better optical insertion loss performance (probably due to a more matured fabrication process on a silicon substrate) with a similar EO response and modulation efficiency, as compared to the TFLN modulator using the same type of electrode on a quartz substrate.[17]

IV. CONCLUSION

In this paper, we have demonstrated TFLN based EO modulators using the CLTW electrode on a silicon substrate. Experimentally, the devices show a high modulation efficiency $V_\pi L$ of ~2.20 V cm and ultra-low optical and RF losses. The longest fabricated modulator exhibits a V_π of 2.2 V and excellent EO modulation response with a roll-off of 1.4 dB at 67 GHz. Employing the undercut etching technique, we can compensate the slow-wave effect induced by the CLTW electrode on a silicon substrate while maintaining the impedance and index matching. Although such segmented electrode designs have been applied on the TFLN platform on a quartz substrate,[17,20] it is the first time to introduce such a device on a silicon substrate, which makes the proposed modulator compatible with silicon photonic integration circuits. Using a hybrid integration technique, e.g., wafer bonding, a high performance EO modulator using the CLTW electrode on the silicon-LN hybrid platform can also be achieved. In Fig. 7, we plot the predicted EO modulation responses with different V_π values, using the measured modulation efficiency $V_\pi L$ = 2.20 V cm and RF loss α_m in Fig. 5(e) while considering a perfect impedance and index matching between the optical and RF waves. A driving voltage of <1 V and 3 dB bandwidth of >60 GHz can be achieved simultaneously using the proposed device structure. Moreover, combined with the folded modulator design,[23,24] the length of the TFLN modulator discussed here can be largely shortened. Based on the above experimental results and

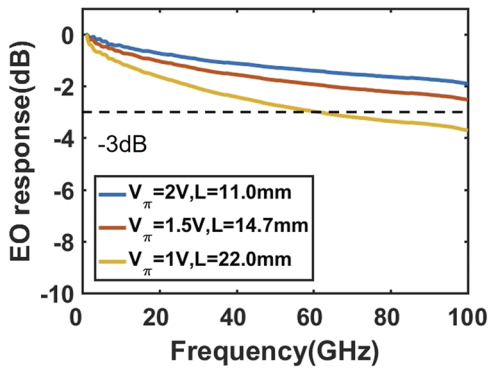

FIG. 7. Predicted EO modulation bandwidth of the proposed device corresponding to different voltages and modulation lengths. The measured $V_\pi L$ = 2.20 V cm and α_m in Fig. 5(e) are adopted here with a perfect impedance and index matching assumed.

analyses; we firmly believe that our demonstration, with the possible integration of other silicon photonic devices, would open up the possibility of achieving sub-1-V driven transmitters supporting a single-lane 100 Gbaud data rate.

ACKNOWLEDGMENTS

The authors acknowledge financial support from the National Research and Development Program (Grant No. 2019YFB2203200), the National Natural Science Foundation of China (NSFC) (Grant Nos. 62135012, 62105107, 91950205, 61961146003, and 92150302), the Guangdong Basic and Applied Basic Research Foundation (Grant No. 2021A1515012215), the Science and Technology Planning Project of Guangdong Province (Grant No. 2019A050510039), and the Fundamental Research Funds for the Central Universities (Grant No. 2021QNA5001).

AUTHOR DECLARATIONS

Conflict of Interest

The authors have no conflicts to disclose.

DATA AVAILABILITY

The data that support the findings of this study are available from the corresponding authors upon reasonable request.

REFERENCES

[1] E. L. Wooten, K. M. Kissa, A. Yi-Yan, E. J. Murphy, D. A. Lafaw, P. F. Hallemeier, D. Maack, D. V. Attanasio, D. J. Fritz, G. J. McBrien, and D. E. Bossi, "A review of lithium niobate modulators for fiberoptic communications systems," IEEE J. Sel. Top. Quantum Electron. **6**, 69–82 (2000).

[2] K. F. Reim, J. Nunn, V. O. Lorenz, B. J. Sussman, K. C. Lee, N. K. Langford, D. Jaksch, and I. A. Walmsley, "Towards high-speed optical quantum memories," Nat. Photonics **4**, 218–221 (2010).

[3] C. Wang, M. Zhang, M. Yu, R. Zhu, H. Hu, and M. Loncar, "Monolithic lithium niobate photonic circuits for Kerr frequency comb generation and modulation," Nat. Commun. **10**, 978 (2019).

[4] Q. Cheng, M. Bahadori, M. Glick, S. Rumley, and K. Bergman, "Recent advances in optical technologies for data centers: A review," Optica **5**, 1354–1370 (2018).

[5] C. R. Doerr, "Direct modulation of long-cavity semiconductor lasers," J. Lightwave Technol. **14**, 2052–2061 (1996).

[6] M. Li, L. Wang, X. Li, X. Xiao, and S. Yu, "Silicon intensity Mach–Zehnder modulator for single lane 100 Gb/s applications," Photonics Res. **6**, 109–116 (2018).

[7] C. Kieninger, Y. Kutuvantavida, D. L. Elder, S. Wolf, H. Zwickel, M. Blaicher, J. N. Kemal, M. Lauermann, S. Randel, W. Freude, L. R. Dalton, and C. Koos, "Ultra-high electro-optic activity demonstrated in a silicon-organic hybrid (SOH) modulator," Optica **5**, 739–748 (2018).

[8] S. Ummethala, J. N. Kemal, A. S. Alam, M. Lauermann, A. Kuzmin, Y. Kutuvantavida, S. H. Nandam, L. Hahn, D. L. Elder, L. R. Dalton, T. Zwick, S. Randel, W. Freude, and C. Koos, "Hybrid electro-optic modulator combining silicon photonic slot waveguides with high-k radio-frequency slotlines," Optica **8**, 511–519 (2021).

[9] C. Koos, J. Leuthold, W. Freude, M. Kohl, L. Dalton, W. Bogaerts, A. L. Giesecke, M. Lauermann, A. Melikyan, S. Koeber, S. Wolf, C. Weimann, S. Muehlbrandt, K. Koehnle, J. Pfeifle, W. Hartmann, Y. Kutuvantavida, S. Ummethala, R. Palmer, D. Korn, L. Alloatti, P. C. Schindler, D. L. Elder, T. Wahlbrink, and J. Bolten, "Silicon-organic hybrid (SOH) and plasmonic-organic hybrid (POH) integration," J. Lightwave Technol. **34**, 256–268 (2016).

[10] A. Melikyan, K. Koehnle, M. Lauermann, R. Palmer, S. Koeber, S. Muehlbrandt, P. C. Schindler, D. L. Elder, S. Wolf, W. Heni, C. Haffner, Y. Fedoryshyn, D. Hillerkuss, M. Sommer, L. R. Dalton, D. Van Thourhout, W. Freude, M. Kohl, J. Leuthold, and C. Koos, "Plasmonic-organic hybrid (POH) modulators for OOK and BPSK signaling at 40 Gbit/s," Opt. Express **23**, 9938–9946 (2015).

[11] Y. Ogiso, J. Ozaki, Y. Ueda, H. Wakita, M. Nagatani, H. Yamazaki, M. Nakamura, T. Kobayashi, S. Kanazawa, Y. Hashizume, H. Tanobe, N. Nunoya, M. Ida, Y. Miyamoto, and M. Ishikawa, "80-GHz bandwidth and 1.5-V V_π InP-based IQ modulator," J. Lightwave Technol. **38**, 249–255 (2020).

[12] M. Lawrene, "Lithium niobate integrated optics," Rep. Prog. Phys. **56**, 363–429 (1993).

[13] M. De Micheli, J. Botineau, P. Sibillot, D. B. Ostrowsky, and M. Papuchon, "Fabrication and characterization of titanium indiffused proton exchanged (TIPE) waveguides in lithium niobate," Opt. Commun. **42**, 101–103 (1982).

[14] J. Kondo, A. Kondo, K. Aoki, M. Imaeda, T. Mori, Y. Mizuno, S. Takatsuji, Y. Kozuka, O. Mitomi, and M. Minakata, "40-Gb/s X-cut $LiNbO_3$ optical modulator with two-step back-slot structure," J. Lightwave Technol. **20**, 2110–2114 (2002).

[15] C. Wang, M. Zhang, X. Chen, M. Bertrand, A. Shams-Ansari, S. Chandrasekhar, P. Winzer, and M. Lončar, "Integrated lithium niobate electro-optic modulators operating at CMOS-compatible voltages," Nature **562**, 101–104 (2018).

[16] M. He, M. Xu, Y. Ren, J. Jian, Z. Ruan, Y. Xu, S. Gao, S. Sun, X. Wen, L. Zhou, L. Liu, C. Guo, H. Chen, S. Yu, L. Liu, and X. Cai, "High-performance hybrid silicon and lithium niobate Mach–Zehnder modulators for 100 Gbit s^{-1} and beyond," Nat. Photonics **13**, 359–364 (2019).

[17] P. Kharel, C. Reimer, K. Luke, L. He, and M. Zhang, "Breaking voltage-bandwidth limits in integrated lithium niobate modulators using micro-structured electrodes," Optica **8**, 357–363 (2021).

[18] Z. Ruan, J. Hu, Y. Xue, J. Liu, B. Chen, J. Wang, K. Chen, P. Chen, and L. Liu, "Metal based grating coupler on a thin-film lithium niobate waveguide," Opt. Express **28**, 35615–35621 (2020).

[19] J. Cai, C. Guo, C. Lu, A. P. T. Lau, P. Chen, and L. Liu, "Design optimization of silicon and lithium niobate hybrid integrated traveling-wave Mach-Zehnder modulator," IEEE Photonics J. **13**, 2200206 (2021).

[20] X. Liu, B. Xiong, C. Sun, J. Wang, Z. Hao, L. Wang, Y. Han, H. Li, J. Yu, and Y. Luo, "Wideband thin-film lithium niobate modulator with low half-wave-voltage length product," Chin. Opt. Lett. **19**, 060016 (2021).

[21] P. O. Weigel, J. Zhao, K. Fang, H. Al-Rubaye, D. Trotter, D. Hood, J. Mudrick, C. Dallo, A. T. Pomerene, A. L. Starbuck, C. T. Derose, A. L. Lentine, G. Rebeiz, and S. Mookherjea, "Bonded thin film lithium niobate modulator on a silicon photonics platform exceeding 100 GHz 3-dB electrical modulation bandwidth," Opt. Express **26**, 23728–23739 (2018).

[22] A. Rao, A. Patil, P. Rabiei, A. Honardoost, R. Desalvo, A. Paolella, and S. Fathpour, "High-performance and linear thin-film lithium niobate Mach–Zehnder modulators on silicon up to 50 GHz," Opt. Lett. **41**, 5700–5703 (2016).

[23] J. Hu, C. Li, C. Guo, C. Lu, A. P. T. Lau, P. Chen, and L. Liu, "Folded thin-film lithium niobate modulator based on a poled Mach–Zehnder interferometer structure," Opt. Lett. **46**, 2940–2943 (2021).

[24] S. Sun, M. Xu, M. He, S. Gao, X. Zhang, L. Zhou, L. Liu, S. Yu, and X. Cai, "Folded heterogeneous silicon and lithium niobate Mach–Zehnder modulators with low drive voltage," Micromachines **12**, 823 (2021).